AQ

An Investigation of the Flowfield for an Integrated Airframe/Propulsion System

by

Alois F. Kreins

Final Report

EOARD CONTRACT F61708-97-W0084

1 Apr - 30 Sep 1997

Department of Aeronautics
U. S. Air Force Academy
USAF Academy, CO 80840-6222

REPORT DOCUMENTATION PAGE

Form Approved OMB No. 0704-0188

1. AGENCY USE ONLY (Leave blank)	2. REPORT DATE	3. REPORT TYPE AND DATES COVERED
	October 1997	Final Report

4. TITLE AND SUBTITLE

An Investigation of the Flowfield for an Integrated Airframe/Propulsion System

5. FUNDING NUMBERS

F6170897W0084

6. AUTHOR(S)

Dr Alois Kreins

7. PERFORMING ORGANIZATION NAME(S) AND ADDRESS(ES)

USAFA/DFAN
2354 Fairchild Drive
Colorado Springs 80840
USA

8. PERFORMING ORGANIZATION REPORT NUMBER

N/A

9. SPONSORING/MONITORING AGENCY NAME(S) AND ADDRESS(ES)

EOARD
PSC 802 BOX 14
FPO 09499-0200

10. SPONSORING/MONITORING AGENCY REPORT NUMBER

SPC 97-4029

11. SUPPLEMENTARY NOTES

12a. DISTRIBUTION/AVAILABILITY STATEMENT

Approved for public release; distribution is unlimited.

12b. DISTRIBUTION CODE

A

13. ABSTRACT (Maximum 200 words)

This report results from a contract tasking USAFA/DFAN as follows: The contractor will modify an existing wind tunnel model of a hypersonic vehicle to incorporate devices that permit control of the onset of boundary layer transition. He will conduct comprehensive wind tunnel tests to determine the ct on the forebody flowfield of fixing the transition location.

14. SUBJECT TERMS

Hypersonic Flow Control

15. NUMBER OF PAGES

36

16. PRICE CODE

N/A

17. SECURITY CLASSIFICATION OF REPORT	18. SECURITY CLASSIFICATION OF THIS PAGE	19. SECURITY CLASSIFICATION OF ABSTRACT	20. LIMITATION OF ABSTRACT
UNCLASSIFIED	UNCLASSIFIED	UNCLASSIFIED	UL

Preface

This work was supported by the European Office of Aerospace Research and Development (EOARD) through project contract number F-61708-97-W0084. The work was performed at the USAF Academy, Department of Aeronautics, during the period April 1 - September 30, 1997. The author thanks Capt. M. E. Zuber for his contributions in getting the heat transfer data and Capt. J. E. Mayhew for computing thermodynamic properties associated with the tunnel flow. The author also acknowledges the outstanding highly motivated technical assistance of Mr. L. Lamblin and also greatly appreciates the outstanding support of the model builders Bobby Hatfield and Jim Philp. My thanks to all the staff of the USAF Academy Aeronautics Laboratory for their helpfulness, co-operation and the pleasant working atmosphere.

Abstract

Sponsored by the European Office of Aerospace Research and Development (EOARD), a hypersonic Airframe/Propulsion Integration (API) configuration has been experimentally investigated in the U. S. Air Force Academy's Tri-Sonic wind tunnel (TWT), and numerically supported by computer simulations made using the General Aerodynamic Simulation Program (GASP). The entire test program, conducted from 1 April 1997 to 30 September 1997, was divided in two test phases as described below.

The first phase of the research program included the design of an API configuration. This configuration was designed in such a manner to provide a flowfield giving the essential flow phenomena to be simulated in the TWT. The first step was to compute flowfield solutions for model geometries at test conditions for the Tri-Sonic Wind Tunnel. Computed flowfields generated using the GASP code were then used to determine the configuration geometry for the desired flowfield. The wind-tunnel model represents only that portion of the vehicle from the nose to the inlet of the API system. The primary variables include the leading-edge nose radius, the angle of the wedge ramp, and the geometry of the isentropic compression surface. The model was exposed to a free stream Mach number of 4.28 with a unit Reynolds number of approximately one million per inch. Schlieren photographs, oil flow patterns, surface and pitot pressure measurements at zero angle of attack were obtained.

The primary objective of the second phase of the research program was to determine the effect on the forebody flowfield of fixing the transition location. Concerning this, the Phase I wind tunnel model was modified to accommodate devices used to control the onset of the boundary layer transition. Thermochromic liquid-crystals (TLCs) were used to provide qualitative information about flow structures on the model surface. Using the TLC temperature distribution at different times, heat transfer coefficients were determined to identify the region of transition. Results showed that natural transition occurred approximately between 28 to 38 percent of model length, but seemed to stay transitional beyond the end of the model. Tripping the boundary layer with roughness elements caused the onset of transition to move forward, close to the trip location. Since the calculated boundary layer was approximately 0.016 inches at the trip location, even a trip element height of 0.01 inches promoted transition at the trip location, and the boundary layer stayed transitional beyond the rear of the model. A turbulent boundary layer at the inlet face has not been achieved for the test conditions, not even for the large roughness elements used in this study.

Contents

Nomenclature

a	Thermal diffusivity of the material
c_w	Specific heat of the wall
$c_{p,Air}$	Specific heat of air at constant pressure
d	Diameter of roughness element
h	Heat transfer coefficient
k	Height of roughness element
k_w	Thermal conductivity of the wall
L	Model Length, L = 12 inches
M	Mach number
M_l	Local Mach number
p	Static pressure
p_{tl}	Total pressure in the tunnel reservoir
$\dot{q}_w$	Heat flux into the wall
Re_l	Unit Reynolds number per ft $Re = \rho_l u_l / \mu_l$
Re_k	Reynolds number based on conditions at boundary layer edge and height of roughness $Re_k = \rho_e u_e k / \mu_e$
$Re_{k,eff}$	Reynolds number based on conditions at boundary layer edge and effective trip size k_{eff}, $Re_{k,eff} = \rho_e u_e k_{eff} / \mu_e$
Re_{xk}	Reynolds number based on conditions boundary layer edge and distance from leading edge to roughness position, $Re_{xk} = \rho_e u_e x_k / \mu_e$
St	Stanton number, see eq. 6
t	Time
T	Temperature
T_{tl}	Total temperature in the tunnel reservoir
x_k	Distance from leading edge to roughness position
x_T	Distance from leading edge to position where boundary layer becomes turbulent
x, y, z	Coordinates in x, y and z direction
α	Angle of attack
β	Non-dimensional, heat transfer parameter determined empirically from eq. 4
δ_k	Undisturbed boundary-layer thickness at the location of roughness element
ρ_w	Density of the wall

Subscripts

am	Adiabatic wall conditions
e	Conditions at boundary layer edge
l	Freestream conditions
l	Local
0	Initial conditions

Abbreviations

API	Airframe/Propulsion Integration
CAD	Computer-Aided Design
CAM	Computer-Aided Manufacturing
CNC	Computer Numerically Controlled
EOARD	European Office of Aerospace Research and Development
GASP	General Aerodynamic Simulation Program
PMEL	Precision Measurement and Equipment Laboratory
PNS	Parabolized Navier-Stokes
TLC	Thermochromic Liquid Crystal
TLNS	Thin-Layer Navier-Stokes
TWT	Tri-Sonic Wind Tunnel

List of Figures

List of Tables

1. Introduction

The successful integration of an airframe/propulsion system presents a serious challenge to high speed vehicle designers and requires intensive research since the forebody's geometry significantly influences the performance of the overall vehicle[1-4]. Vehicle stability, aerodynamic characteristics, and propulsion are just a few design issues that have to be considered. Specifically, the forebody geometry is critical to the integration process, and it should be designed with the following features: (1) A two dimensional flow approaching the inlet (i.e., a flow with small transverse variations across the inlet face). Moreover, a two dimensional flow with a stable turbulent boundary layer devoid of strong flow interactions (shock-boundary layer interactions, separation) is needed to have an acceptable lift-to-drag ratio. (2) A small Mach number and high static pressure for the inlet entry flow is needed. (3) A large air mass flow rate entering the engine diffuser is needed to reduce the engine size there by reducing the vehicle drag and total pressure losses, and to maximize the total kinetic energy. (4) Lastly, the guidelines developed in previous programs[1-4], indicate that the API configuration should have a non-circular cross section, a large planform area, and a flat bottom.

At hypersonic speeds, a turbulent boundary layer exists over most of the flight vehicle, yet laminar flow exists over large parts of scaled wind tunnel models at similar speeds. In many ground-test programs, Reynolds-number conditions associated with the model length scale factor and with the test conditions can not match flight conditions, so boundary layer trips are used to initiate transition. However, trip-induced flowfield disturbances which are sufficient to significantly promote the onset of boundary layer transition for supersonic/hypersonic flows may produce unacceptable disturbances to the flow external to the boundary layer. Since these vortical, viscous/inviscid interactions can perturb the flow far downstream of the trip locations, they may degrade the flow entering the engine flow path, thereby adversely affecting engine performance.

The purpose of this research project is to begin an investigation on the behavior of such flowfields. Both an experimental and a numerical program are being conducted. In the first phase, a wind tunnel model was designed and fabricated using the USAF Academy's 4-axis Computer Numerically Controlled (CNC) mill. Dimensioned sketches of the model geometry are presented in **Fig. 1**. Surface and pitot pressure measurements, oil-flow patterns, and Schlieren photographs were obtained for the model tested in a Mach 4.28 air stream. Numerical simulations made using version 3.0 of the General Aerodynamic Simulation Program (GASPv3)[5] were used to support the physical interpretations of the experimental data.

In the second phase of the test program, the wind tunnel model of Phase I was modified to accommodate various types of roughness elements. Positioned on the forebody's lower side close to the leading edge in one and two rows, cylindrical tripping devices of different sizes were chosen for triggering transition with the goal of controlling the transition location without degrading the inviscid external flow. Surface pressure measurements and Schlieren photographs were obtained for the same test conditions mentioned in Phase I. Additionally, heat transfer measurements using Transient liquid-crystals (TLCs) were obtained. To identify the onset

transition, heat transfer coefficients determined from the TLC temperature data at different times were obtained.

a.

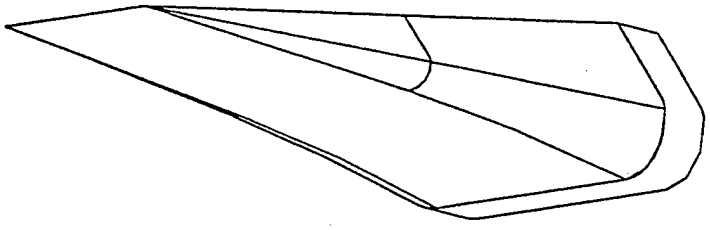

b.

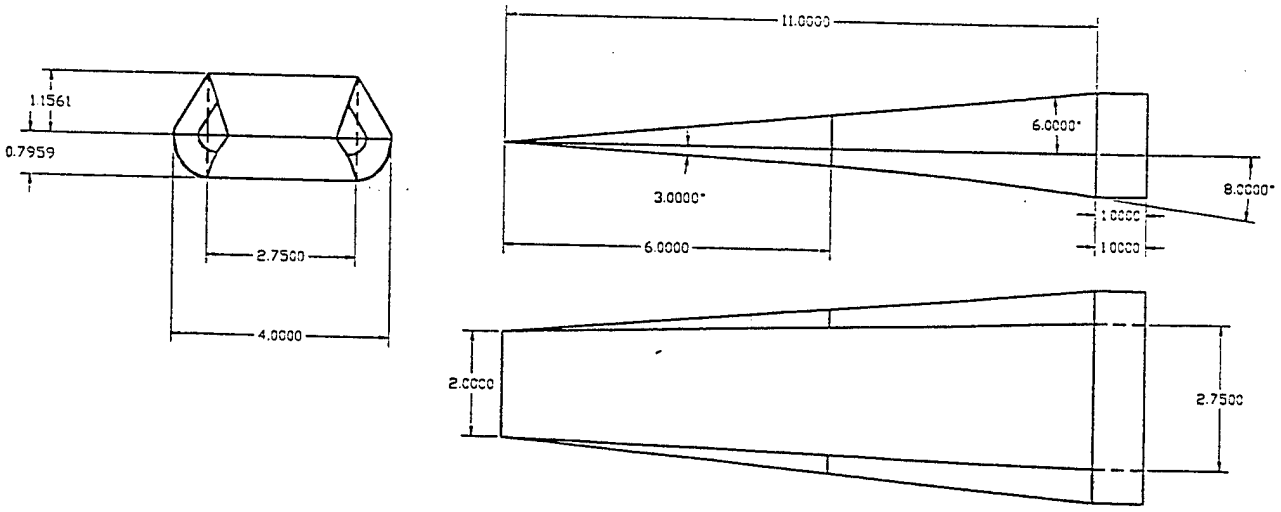

Figure 1: Sketches of the Integrated Airframe/Propulsion configuration (APIC) (all dimensions in inches) (a) Rotated view of the model (b) Three orthogonal views of the model

2. Experimental Program

2.1 Facility

The experimental investigations were conducted in the U. S. Air Force Academy's Tri-Sonic wind tunnel (TWT), schematically shown in **Fig. 2**. This blow down facility is capable of producing nominal test section Mach numbers in the range of 0.14 to 4.38. Discrete Mach numbers in this range are obtained by using different interchangeable convergent-divergent nozzles, each having an exit area (test section area) of 1 foot (0.3048 m) by 1 foot (0.3048 m).

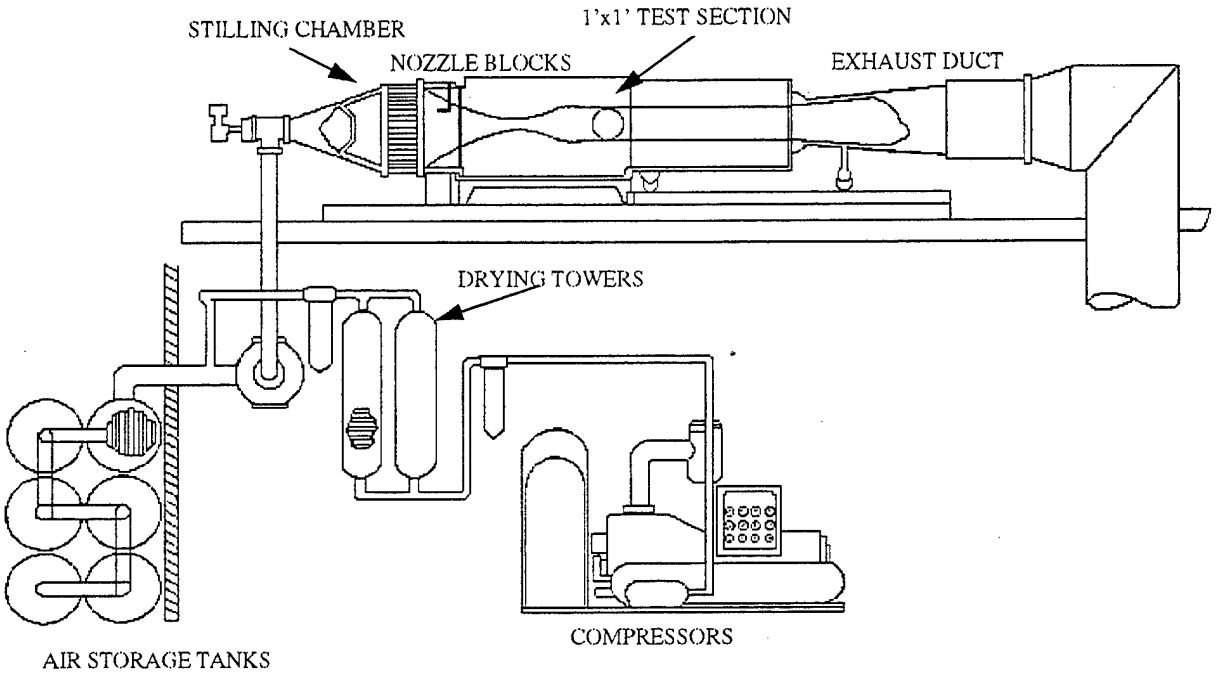

Figure 2: Schematic of USAF Academy Tri-Sonic Wind Tunnel

The run time is a function of the total temperature (T_{tl}), the total pressure in the tunnel reservoir (p_{tl}), and the nozzle throat area (which, since the cross-section area of the test section is fixed, relates uniquely to the Mach number in the test section). Operating run times range from 20 seconds to 420 seconds. The operating conditions for the TWT, including the range of pressure limits for a given Mach number, are presented in **Fig. 3**.

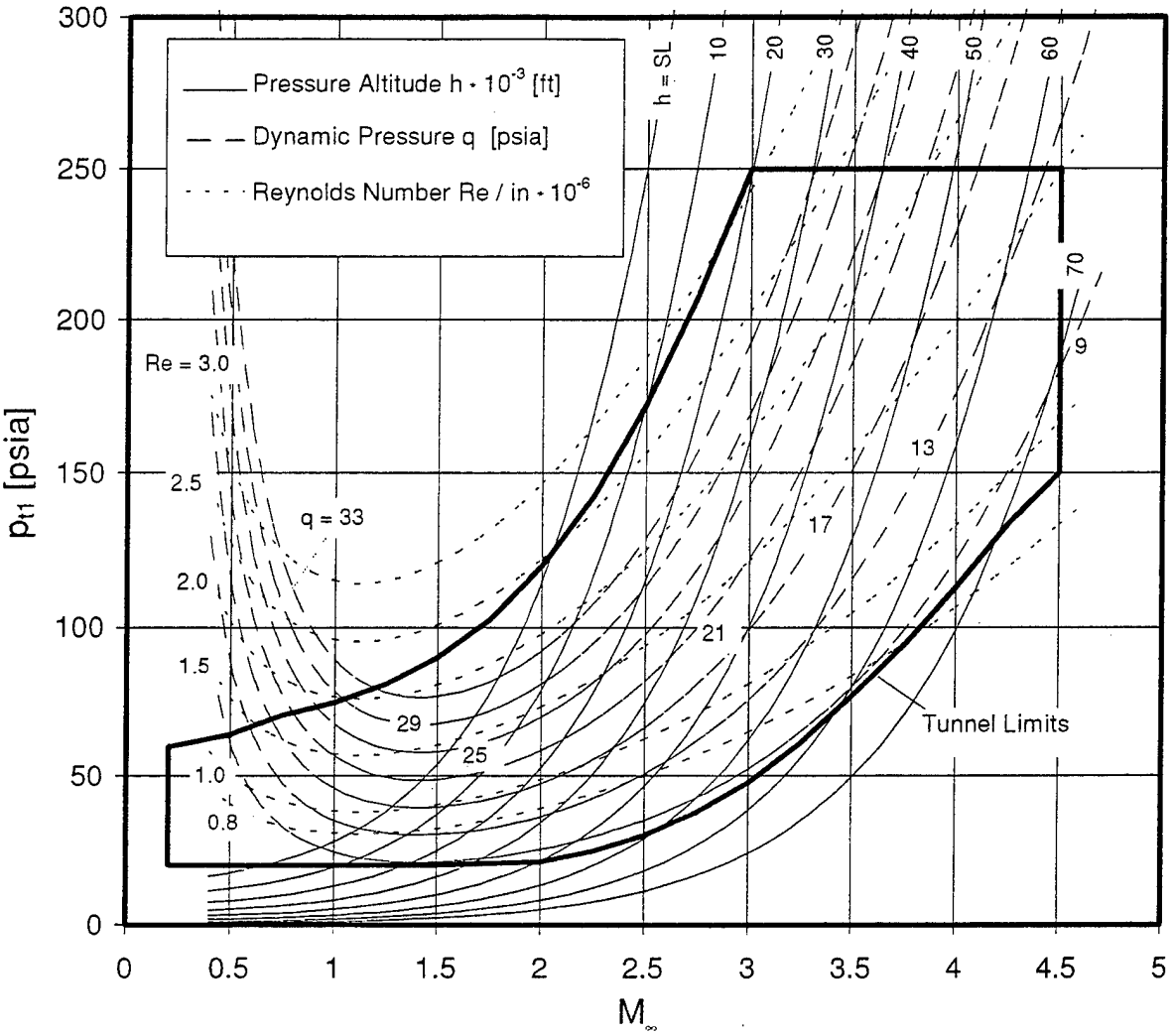

Figure 3: Operating range of TWT hypersonic wind tunnel

2.2 Model

The model of a hypersonic configuration was designed in such a manner that the essentially-desired flow phenomena have been simulated in the TWT. Large starting loads are imposed on the wind tunnel model for the test conditions used. Therefore, a stress analysis of the model and the support was done prior the test. Loads calculated using GASP were applied to the model. Another important consideration is the maximum model size allowable for tunnel starting. If the normal shock that moves down the test section from the nozzle does not pass across the model during the starting process, the tunnel will choke. In accordance with experimental data on maximum model size for tunnel starting taken from several high-speed wind tunnels[6], a model (Fig. 1) with a length of 12.00 inches, a width of 4 inches, and a height of 2 inches has shown to be acceptable for the TWT tests.

The geometry of the API model was created by using the parametric, feature-based solid-modeling CAD system AutoCad® 13 and Autodesk Mechanical Desktop® 1.0. Upon completion of the mechanical design, tool paths have to be generated and post-processed for the machining on the Academy's 4-axis CNC mill. To avoid loss of information caused by the transfer of data between different CAD systems, the CAM package HyperMill® was used. Working as an add on integrated in the same AutoCad environment, tool paths for 3D Z-level roughing and 3D finishing were generated. A wood prototype model was fabricated to ensure that the desired geometry was properly reproduced.

To meet different needs, two geometrically identical wind-tunnel models, consisting of different materials, were built. The first model (API-I), made of aluminum, was built with 30 surface pressure orifices. The locations of these pressure orifices on the AFP-I model are given in **Table 1** (see also **Fig. 4**) in terms of the dimensionless distance from the nose downstream of the model (x/L) and from the centerline spanwise to the main flow direction (z/L). Fourteen of the orifices were located in the plane of symmetry (centerline), starting near the nose and ending on the bottom surface of the flow path for the airbreathing propulsion system. For heat transfer measurements, a transient liquid-crystal technique was used. To ensure acceptable data, the material needs a low thermal conductivity to slow down the heat transfer rates. Accordingly, a second model (API-II) with Plexiglas™ was fabricated.

Table 1: Locations of pressure orifices on the API-I model

Orifice No.	x/L	z/L
1	0.0833	0.0
2	0.1667	0.0
3	0.2499	0.0
4	0.2499	+0.0417
5	0.2499	+0.0833
6	0.3333	0.0
7	0.4167	0.0
8	0.5000	0.0
9	0.5750	0.0
10	0.5750	0.0417
11	0.5750	0.0833
12	0.6583	0.0
13	0.7416	0.0
14	0.8250	0.0
15	0.9083	0.0

Orifice No.	x/L	z/L
16	0.9250	0.0
17	0.9583	0.0
18	0.9917	0.0
19	0.9083	-0.1
20	0.9083	-0.0833
21	0.9083	-0.0667
22	0.9083	-0.0500
23	0.9083	-0.0333
24	0.9083	-0.0167
25	0.9083	+0.0167
26	0.9083	+0.0333
27	0.9083	+0.0500
28	0.9083	+0.0667
29	0.9083	+0.0833
30	0.9083	+0.1

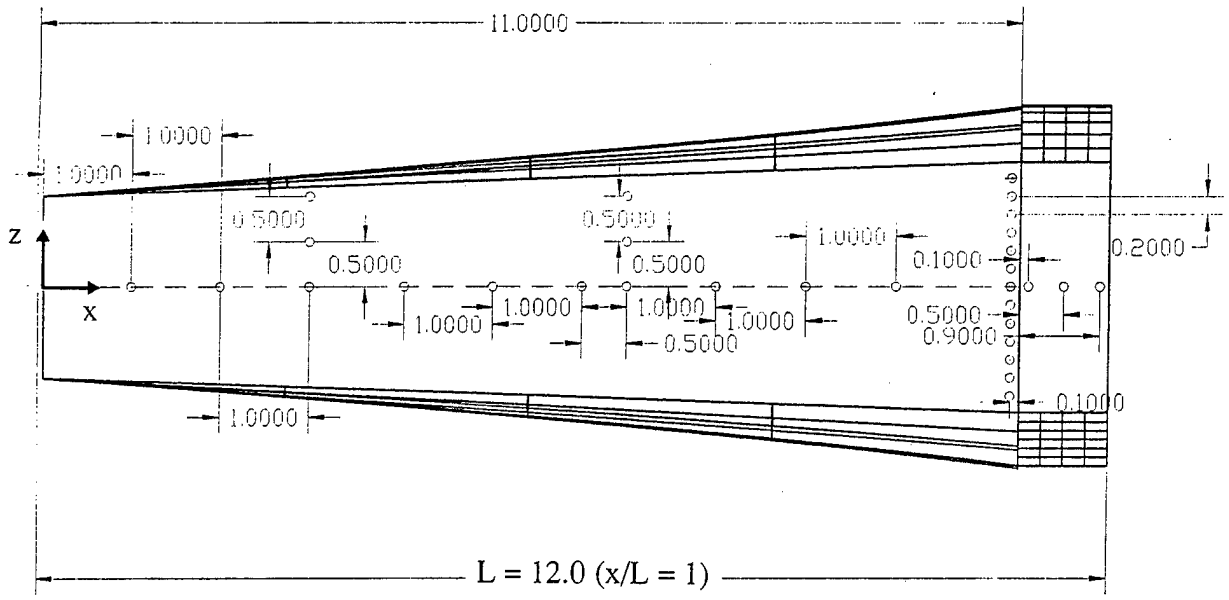

Figure 4: Bottom view of the API-I wind tunnel model with pressure tap locations (all dimensions in inches)

2.3 Instrumentation

2.3.1 Tunnel Instrumentation

The total pressure in the stilling chamber was measured by a transducer having a full-scale range of 300 psia (2.068×10^6 N/m^2) with a combined nonlinearity and hysterises of $\pm$ 0.3% full scale. The maximum total pressure in the stilling chamber, which occurs at the higher Mach numbers (see Fig. 3), is 250 psia (1.724×10^6 N/m^2). The total temperature in the stilling chamber was measured by a Type E (chromel/constantan) thermocouple capable of measuring -328°F to 1652°F (-200°C to 900°C) with a sensitivity of 67.9 μV/°C. The total temperature could be varied only slightly, being 560°R (311K) $\pm$20°R ($\pm$11K).

2.3.2 Model Instrumentation

2.3.2.1 Pressure Instrumentation

Static pressures were measured at 30 locations on the model identified in Fig 4. The pressure orifices used stainless steel tubing with an inside diameter of 0.0310 in. (0.787 mm). Through approximately ten feet (3.05 m) of tygon tubing with an inside diameter of 0.0313 in. (0.794 mm) and an outside diameter of 0.0938 in. (2.38 mm) the pressures then passed to a pressure transducer embedded inside a scani-valve. For the present pressure measurements, a Kulite model XT-190-15D differential-pressure transducer with a full-scale range of 15 psid (1.03×10^5 N/m^2,

differential) and a combined nonlinearity and hysterises of ± 0.5% full scale was used. The reference (atmospheric) pressure was measured by a Heise digital pressure indicator with a full-scale range of 17.19 psia. Including the effects of sensitivity, hysterises, nonlinearity, and repeatability, the atmospheric pressure measurement had an uncertainty of ±0.035% of the full-scale measurement at 70 °F (21 °C). Because of the long length of tygon tubing connecting the pressure orifice in the model to the scani-valve/transducer, all pressure measurements were time-averaged, "steady-state" values. Once the flow was established, a delay time of 4 sec was used before the first port of the scani-valve was recorded, and a 0.2 sec delay between each of the subsequent steps based on previous investigations[7].

2.3.3 Pitot pressure instrumentation

In order to measure the total pressures in the boundary layer and in the external flow, a multiple pitot pressure probe was used which was designed to meet the following requirements (Wuest[28]):

- Boundary layer measurements with as little disturbance as possible.
- No mutual influence between the pressure measurement tubes.

Fig. 5 shows the pitot rake and, diagrammatically, the set-up of the pressure measuring system. The individual pressure measuring tubes, with an outer diameter of 0.043 inches (1.06 mm) and an inner diameter of 0.032 inches (0.81 mm), were arranged at a distance apart of 0.25 inches (6.35 mm). In order to increase the accuracy of the measured values in the direction crosswise to the main flow direction, the pitot tubes were flattend thereby forming an oval shape as indicated in Fig. 5. Differential pressure sensors with a measurement range of 15 psid (≡ 103 kPa) were used for the investigation.

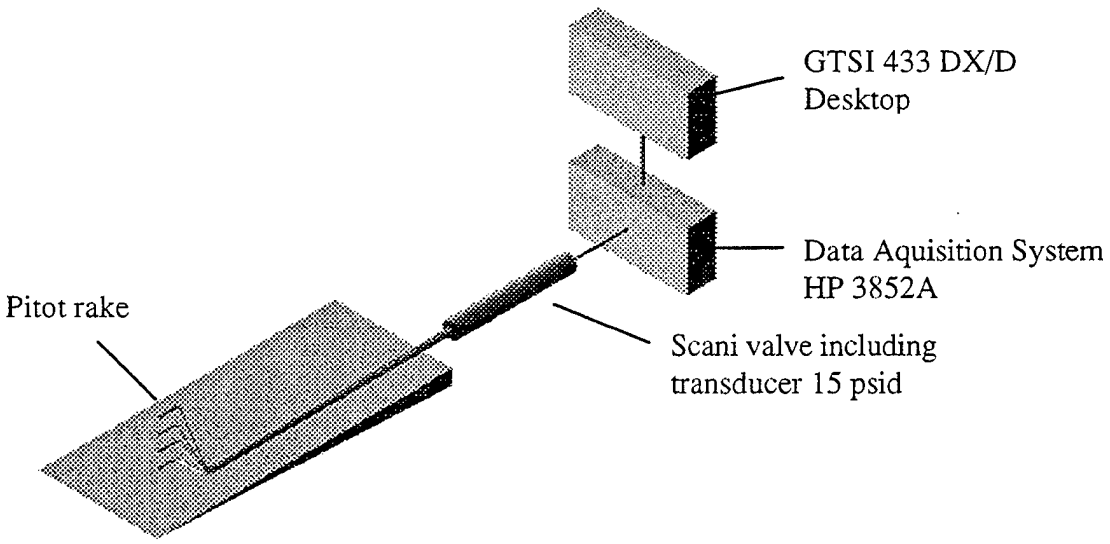

Figure 5: Pitot rake and diagrammatic set-up of the pressure measuring system.

As reported in Ref. 21 pitot pressure measurements have been successfully used for the determination of the state of the boundary layer, i.e. whether laminar, transitional or turbulent. Therefore, the first tube was located near the surface and movable in main flow direction. On being moved downstream the centerline across the transition region, the a pitot tube shows a sudden increase in the total pressure indicating the beginning of the transition region[32].

2.3.3.1 Transient liquid-crystals

Liquid crystals (LCs) were used to provide information about the flowfield on the lower surface of the API-II model. LCs are substances which in certain phases have the mechanical properties of a liquid and optical properties of a crystal. Two types of liquid crystals are shear sensitive or thermochromic (temperature) sensitive. Thermochromic liquid crystals (TLCs) were used in the present experimental program, specifically, a Hallcrest 12C6W TLC with a 5°C bandwidth and a color play starting at 13°C and ending at approximately 18°C. By using a TLC with a specific, wide color-play band, the temperature evolution for specific times and the surface areas can be recorded, when the temperature on the model surface passes through the mentioned temperature range. With this information, qualitative information about the flow near the model surface can be obtained to identify the onset of boundary-layer transition, and the regions where the flow has separated from the surface, these data can also be used to determine the magnitude of the local heat transfer. Several studies have been accomplished using LCs to quantify the aerothermodynamic environment of models exposed to high-speed flows[14, 15].

To optimize the information obtained using TLCs, the model must be constructed of a material with proper thermal conductivity, density, and specific heat. The model used in the present tests was constructed of Plexiglas™ (API-II). The test surface was first air brushed with black paint and then with a coating of the TLC. A Sony XC-003 RGB camera and a Matrox Meteor RGB frame grabber captured the images during the run. The images were grabbed at a specified time schedule. A Micron 166 MHz PC with 128 MB of RAM stored the images until transfer to the hard drive was completed. Images were stored in a TIFF 6.0 format in 24 bit color RGB with a resolution of 640x480. Imaging95 was used to convert the TIFF 6.0 images to TIFF 5.0.

The method used to calculate the heat flux, $\dot{q}_w$, into the structure assumes that the surface temperature, T_a, i.e. the initial temperature of the model, at the beginning of the test and the wall temperature, T_w, at a certain time, t, are available. The following assumptions also apply:

- The material values, i.e. the thermal conductivity, k_w, the density, ρ_w, and the specific heat, c_w, of the model are independent of temperature.
- A homogeneous temperature, T_a, applies to the entire model at the beginning of the test.
- The heat does not penetrate deeply into the interior of the surface so that the assumption of a "semi-infinite wall" can be taken as a boundary condition.
- The propagation of heat tangential to the surface is neglected and this, therefore, permits the one dimensional treatment of the heat conduction equation.
- No heat sources exist.

With these assumptions the transient thermal conductivity equation (Fourier equation) becomes

$$\frac{\partial T}{\partial t} = a \cdot \frac{\partial^2 T}{\partial y^2} \tag{1}$$

with the thermal diffusivity of the material

$$a = \frac{k_w}{\rho_w \cdot c_w} . \tag{2}$$

Using the solution of Eq. (1)[31]

$$\frac{T_w - T_{aw}}{T_{w,0} - T_{aw}} = e^{\beta^2} \operatorname{erfc}\beta \tag{3}$$

where

$$h = \frac{\beta\sqrt{\rho_w c_w k_w}}{\sqrt{t}}, \tag{4}$$

the heat transfer coefficient can be iteratively determined at the position for y = 0, i.e. on the surface. Using this method, the wall heat flux is determined as

$$\dot{q}_w = h \cdot (T_{aw} - T_w) \tag{5}$$

with the adiabatic wall temperature T_{aw} and h the heat transfer coefficient.

A non-dimensional heat transfer coefficient, the Stanton number St, is used to give the thermal loads. Neglecting the thermal radiation for the flow conditions used the Stanton number is:

$$St = \frac{\dot{q}_w}{\rho_1 \cdot u_1 \cdot c_{p,Air} \cdot (T_{aw} - T_w)} . \tag{6}$$

2.4 Test Conditions

The freestream Mach number in the test section was 4.28±0.04. This is the average value determined from a facility calibration program in which an eleven probe pitot rake was rotated in 30° increments. These pitot-pressure measurements were used to generate Mach number contours for three planes in the test section: one at the upstream end, a second in the middle, and the third at the downstream end of the test section. This value has been verified in repeated investigations of the flow quality of the TWT.

The perfect-gas relations were used to calculate the freestream conditions, assuming that the flow accelerated isentropically from the nominal stagnation conditions to the Mach 4.28 freestream. Sutherland's equation[13] was used to calculate the freestream viscosity. The mean wind-tunnel test conditions for the experimental investigation are summarized in **Table 2.**

Table 2: Mean wind tunnel test conditions

M	α [°]	p_{t1} [psia]	T_{t1} [°F]	p_1 [psia]	Re [10^6 / ft]
4.28	0	150	87.28	0.683	11.77
4.28	0	177	89.74	0.809	13.87
4.28	0	205	93.31	0.939	15.92
4.28	0	234	91.94	1.062	18.18

2.5 Uncertainty Aanalysis

The overall measurement uncertainties are estimated using the methods described in Refs. 8, 9, 10, 11. After determining the bias error B and the precision error P individually, the root-sum-square (RSS) method was used to combine to obtain the total uncertainty U_{RSS}:

$$U_{RSS} = \pm\sqrt{B^2 + P_{\bar{x}}^2} \tag{7}$$

with $P_{\bar{x}} = t_{0.025,n-1}\, S_{\bar{x}} = \dfrac{t_{0.025,n-1}\, S_x}{\sqrt{n}}$

and $S_x = \sqrt{\dfrac{1}{n-1}\sum_{i=1}^{n}(x_i - \bar{x})^2}$,

where t is the t-statistic for a two-sided 95% confidence interval, S_x the sample standard deviation and n the number of individual readings x_i and $\bar{x}$ the mean of sample population defined by

$$\bar{x} = \frac{1}{n}\sum_{i=1}^{n} x_i \ . \tag{8}$$

Before each test the pressure transducer was calibrated. A series of known pressures were applied to the transducer allowing the determination of a calibration slope. Thus, the bias estimate was derived from the uncertainty of the working standard (Flexitester calibrated at the Precision Measurement and Equipment Laboratory PMEL) against which the instrument was calibrated. The precision errors were estimated based on the standard deviations, and the t distribution for a 95% confidence level. Estimated uncertainties in the measured pressures are shown in **Table 3.**

The compressed air for the wind tunnel is routed through two drying towers and stored there after in six holding tanks. The dew point of the dried air is -50°F (-45°C), when the tank temperature is 100°F (38°C) and the tank pressure is 600 psia (4.137×10^6 N/m^2). As a result, the absolute humidity of the dried air is less than 2×10^{-6} kg H_2O per kg dry air, and, thus, moisture can be neglected.

Table 3: Specification and estimated uncertainties

Input parameter	Nominal value	U_{RSS} [%]
$p_{orifice}$	3.5 [psia]	±1.0
p_{t1}	150 [psia]	±2.1
Mach	4.28 [-]	±1.0
p_1	0.68342 [psia]	±5.8
$p_{orifice}/p_1$	5.12 [-]	±6.0

3. Numerical Analysis

Using GASPv3[5], the flowfield for the plane of symmetry from the leading edge to the inlet was computed for the Thin-Layer Navier-Stokes (TLNS) equations (for regions containing imbedded subsonic flow) and Parabolized Navier Stokes (PNS) equations (for purely supersonic regions). The TLNS equations are numerically solved using a finite-volume formulation. GASP offers numerous solution options to the user. The inviscid flux vectors were computed to second-order accuracy using van Leer's flux vector splitting technique combined with the min-mod limiter to maintain stability and eliminate numerical oscillations in regions containing large gradients. The two-factor approximate factorization time-integration scheme was used to solve the TLNS equations. Solutions were considered converged when the residual had decreased by three orders of magnitude for pressure calculations. Freestream flow conditions were specified at the inflow and at the farfield boundaries. A second-order extrapolation boundary condition was specified for the downstream, out-flow boundary. Boundary conditions at the surface of the vehicle included a no-slip requirement for the velocity boundary condition and a specified wall temperature for the thermal-boundary condition.

For the computation of the entire 3-dimensional flowfield around the API-model, a grid containing 145×111×65 nodes (as illustrated in **Fig. 6**) was created using the grid generation program Gridgen 12.0[16]. For the computation of the plane-of-symmetry flow of the model, a finer 2-D grid containing 386×129×2 nodes (as illustrated in **Fig. 7**) was used. The far-field boundaries were placed far enough from the vehicle to capture the attached shock wave emanating from the leading edge of the API. The distance to the first grid point off the surface was set to 1×10^{-6} feet (3×10^{-4} mm).

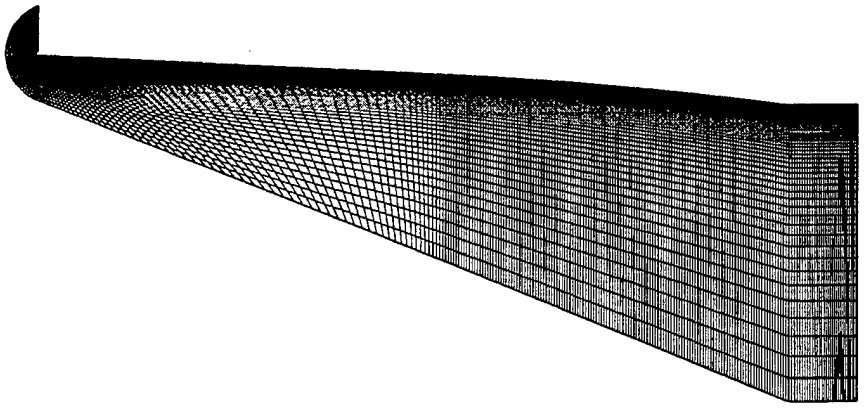

Figure 6: 386×129×2-cell grid used for 2-D GASP calculation (x-y-plane).

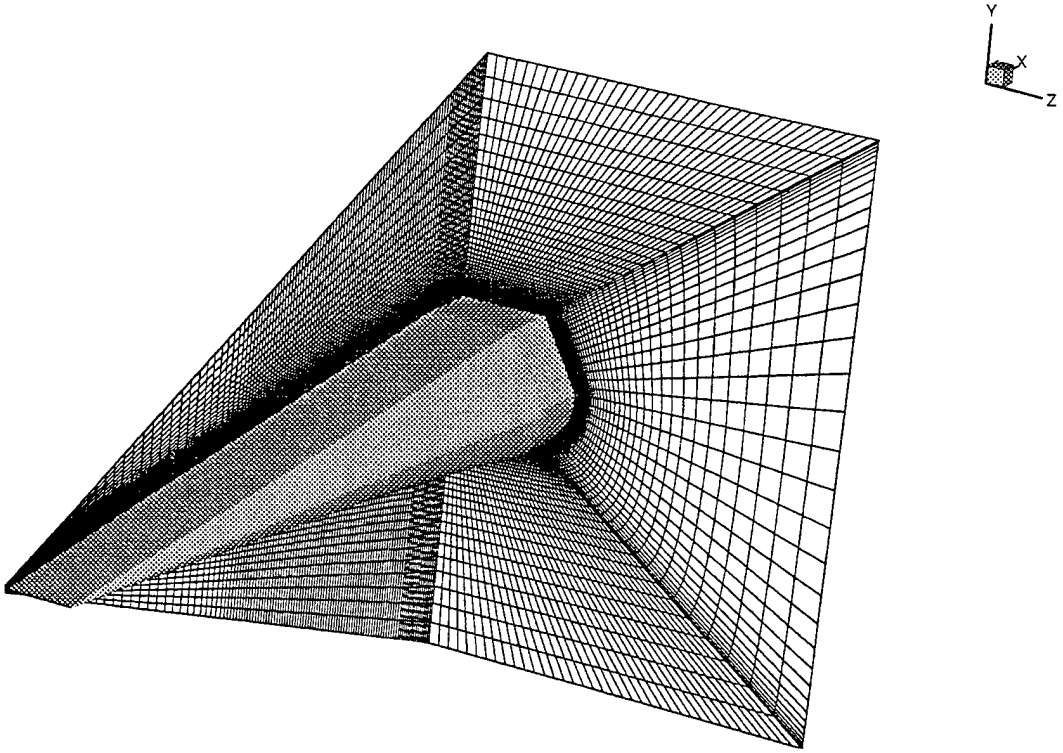

Figure 7: 145×111×65-cell grid used for 3-D GASP calculation.

4. Results and Discussion

4.1 Character of the flowfield approaching the inlet

The character of the forebody flow approaching the inlet strongly effects engines performance. Specifically, the forebody's geometry should be designed in such a manner that the flow approaching the inlet possesses a 2-dimensional character with small distortion across the inlet face. To investigate the flow behavior surface pressures along the centerline were measured and oil and Schlieren photographs were obtained. Numerical simulations of the plane of symmetry and of the entire 3-dimensional flowfield were obtained for supporting the interpretation of the experimental results.

Fig. 8a shows a schlieren image of the flowfield around the API model. **Figure 8b** and **8c** present GASP TLNS/PNS Mach number contours for the plane of symmetry and the 3-D flow field calculated for the same flow conditions as the schlieren results. The computed shock wave overlays the trace of the shock wave in the schlieren photograph.

Pressure distributions, in terms of the dimensionless pressure parameter p/p_1, for the plane of symmetry from the leading edge up to the inlet of the model at zero angle of attack are presented in **Fig. 9**. Since the leading edge has a nose radius of 0.0255 inches, a curved bow shock wave is created in front of the API model, with the shock detached from the nose. The curvature of the bow shock wave causes a reduction in the surface pressure from the leading edge up to the "isentropic" compression ramp at x/L= 0.5, shown for both, the experimental data and the GASP-calculations. Flow instability is another concern of the detached bow shock. This flow structure has the mechanism to be unsteady, thereby further effecting the downstream flow field. For this research, no instrumentation was available to investigate this phenomenon, so the effects of flow unsteadiness are only one item of concern at this time. The pressure ratio calculated using relations in NACA Report 1135[13] shows a lower values in the leading edge region, which is to be expected, since the theory used, assumes an attached bow shock wave to the wedge which is straight. The compression effect of the "isentropic" curved surface from x/L=0.5 to 0.9167 causes the surface pressure to increase and reaches a pressure value of about p/p_1=2.1. Experimental values at this location can not be given since the closest experimental value is located within the inlet flow path, resulting in a pressure drop due to an expansion of the flow.

Surface pressure distributions from the centerline crosswise to the main flow direction in front of the inlet face is presented in **Fig. 10**. Since the pressure orifices are located within the inlet flow path, the measured pressure values are lower than the values in front of the inlet due to the expansion of the flow. The comparison of the experimental data with simulated pressure values located both at the compression ramp and within the inlet flow path indicate a nearly two-dimensional behavior, except for slightly 3-D effects at the outer regions of the inlet face ($-0.1 < z/L < -0.06$, $0.06 < z/L < 0.1$). The two dimensional character is also shown in the oil flow pattern and in the calculated streamlines on the model surface presented in **Fig. 11**.

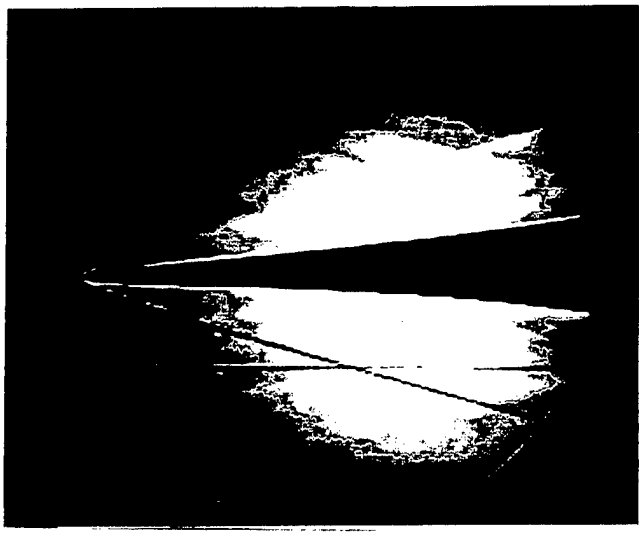

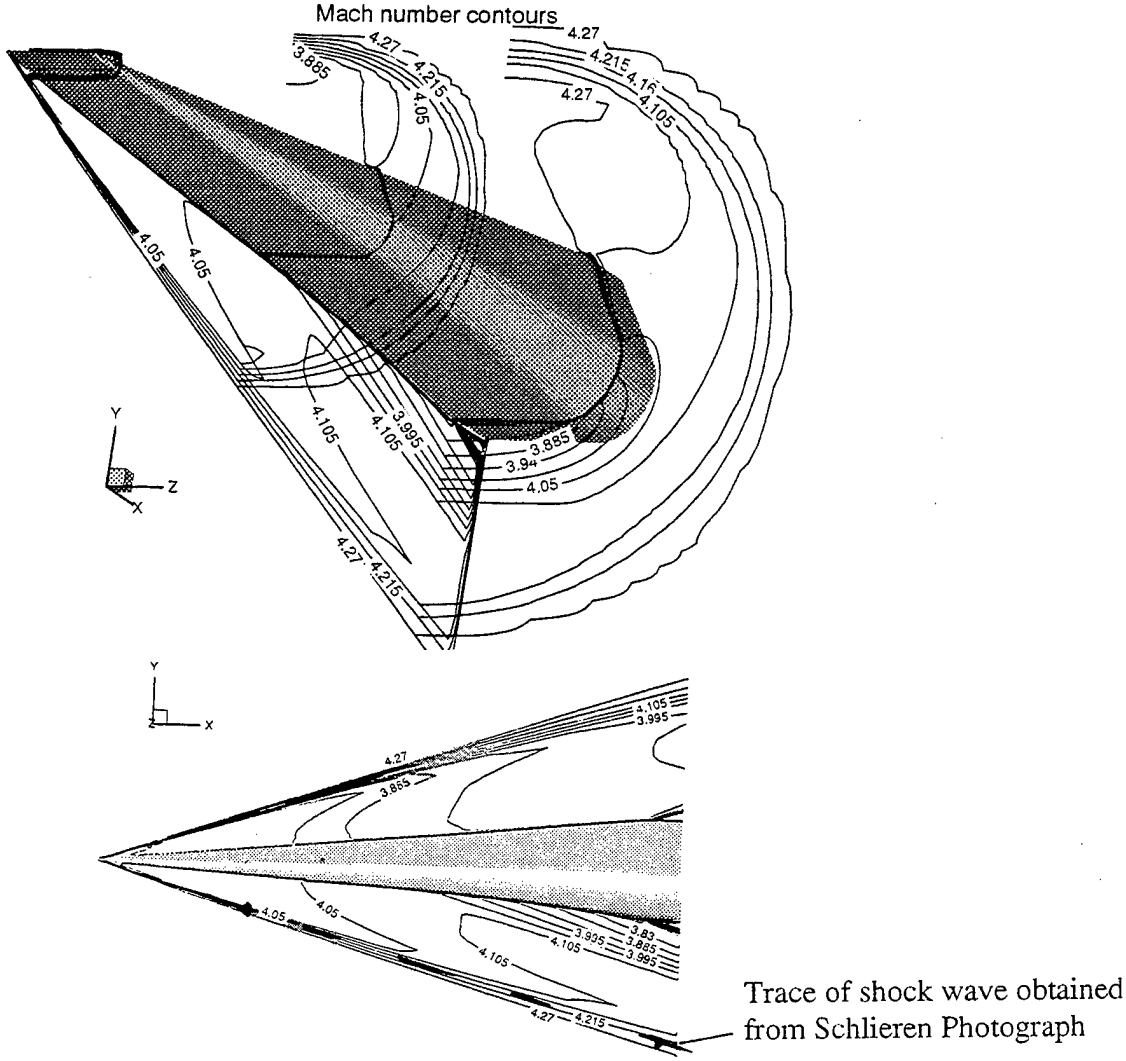

Figure 8: (a) Schlieren image of the flowfield around the API model and (b) Mach number contours from TLNS/PNS 3-D calculations by GASP code (both at $M_\infty = 4.28$, $Re_\infty = 15.92 \times 10^6$ / ft, $\alpha = 0°$.

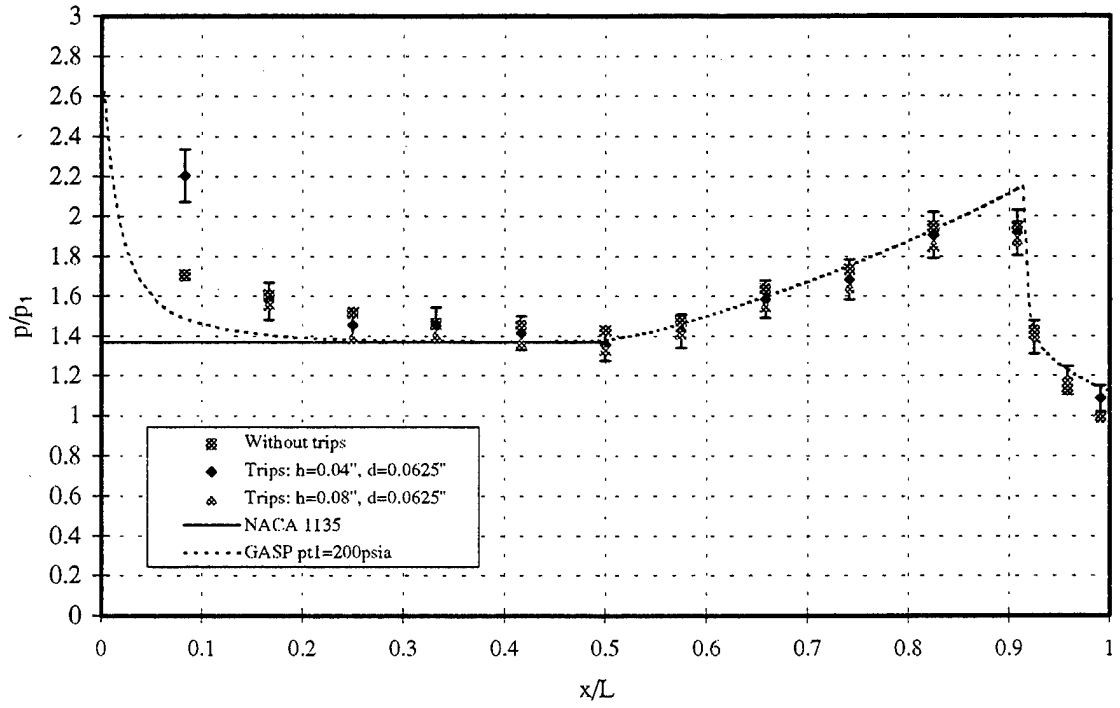

Figure 9: Pressure distribution along the centerline of the API-I model with and without trips (L=12 inches).

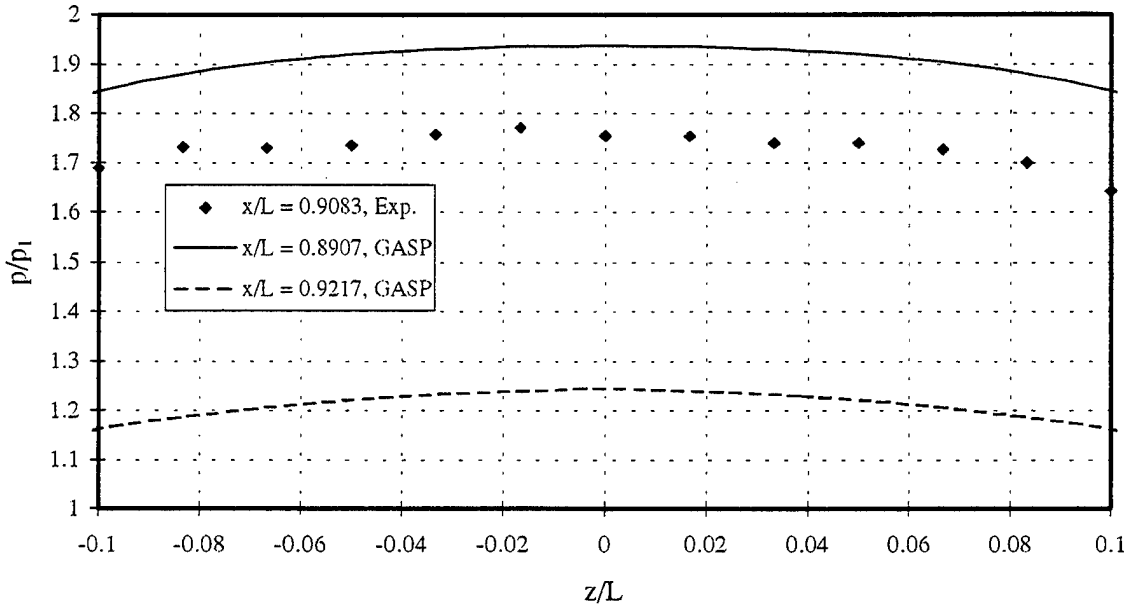

Figure 10: Surface pressure distributions crosswise to the main flow direction in front of the inlet of the API model (p_{t1}=205psia, T_{t1}=93.31°F,Re_L=15.92 $\times 10^6$) .

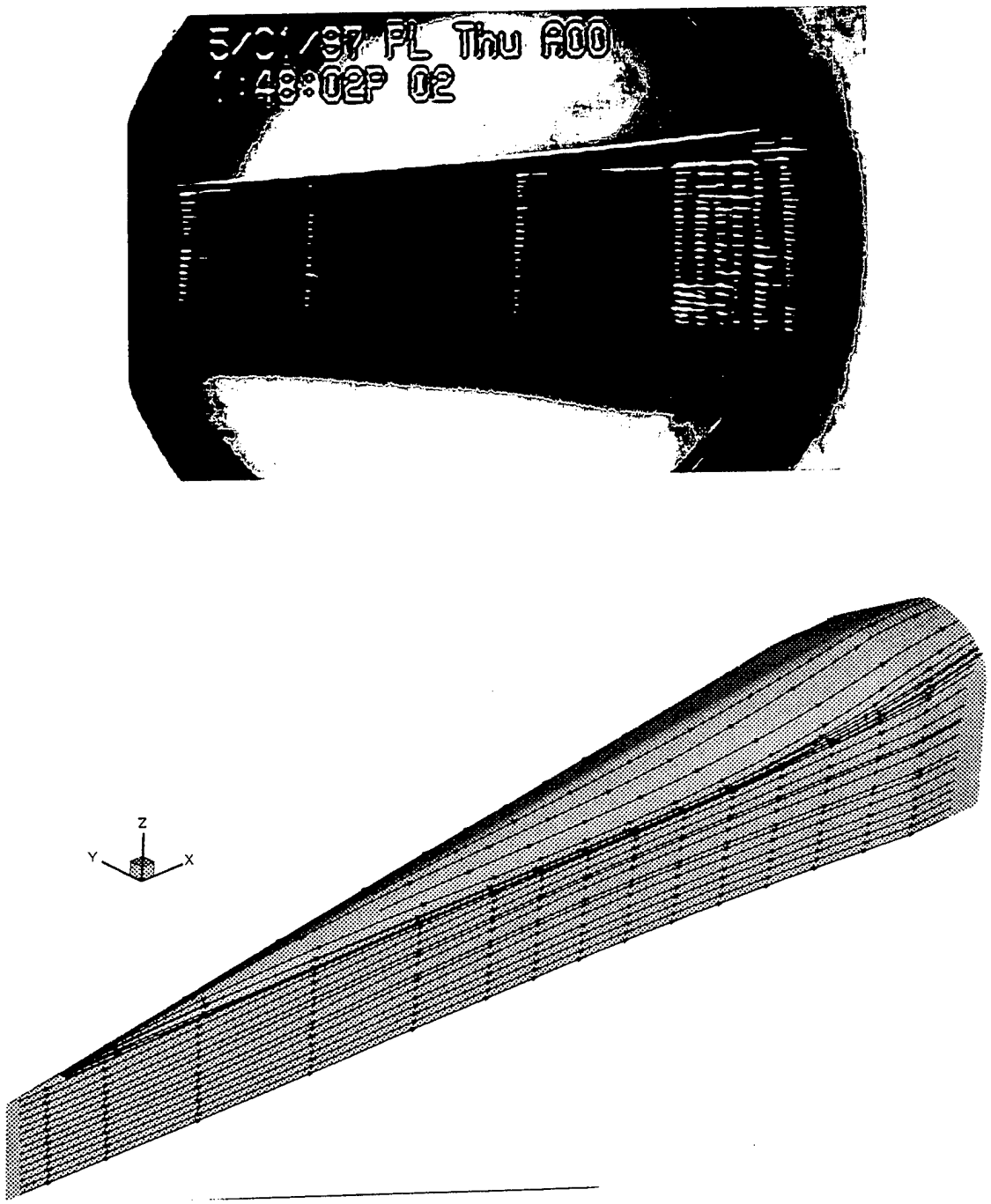

Figure 11: (a) Oil flow pattern and (b) computed contour streamlines on the lower side of the forebody surface of the API-I model.

4.2 Effect of boundary layer tripping devices on transition

4.2.1 Required type, size and location of tripping devices

Full scale free-flight vehicles often experiences largely turbulent boundary-layer flow. On small scale wind tunnels models, however, natural transition to turbulent boundary layers often may not occur due to a Reynold number being to low. As reported[18-22] it is boundary layer tripping devices one used to trigger transition even at low Reynolds number.

Roughness elements introduced into a nominally two-dimensional boundary layer create vortices wrapped around the roughness element as demonstrated in **Fig. 12** taken from Arnal[30]. At a distance x_T from the tipping device, the legs of the vortices break down and form a turbulent boundary layer. When the height k of the protuberance increases, investigations of numerous authors[20, 21, 23] show that x_T decreases up to a minimum value which is reached for an "effective" roughness size k_{eff}. The value k_{eff} and the Reynolds number Re_{keff} formed with the effective roughness height, is of great importance for successfully triggering a laminar to a turbulent boundary layer at a defined location.

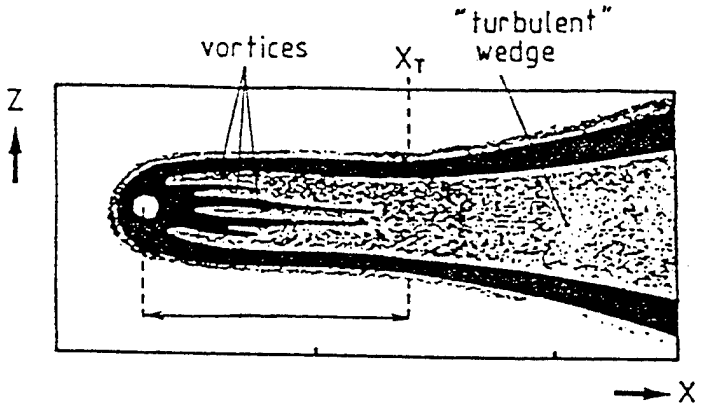

Figure 12: Example of wall visualization on the model surface behind a roughness element using thermosensitive paint as taken from Arnal[30].

In comparison to subsonic flows, in which the selection of an effective tip size k_{eff} are reasonably well established, the choice of an effective tripping device in supersonic and hypersonic flows is complicated. Numerous authors reported[18, 27] that beside the "effective" roughness size k_{eff} and the effective Reynolds number Re_{keff} additional, important roughness-transition parameters, as listed below, have to be considered:

- Model configuration
- Unit Reynolds number
- Local Mach number
- Roughness-height Reynolds number Re_k
- Roughness position Reynolds number Re_{xk}
- Type of roughness
- Spacing of roughness
- Wall temperature
- Pressure Gradient

Roughness-height and roughness position Reynolds number

Morrisette[21] and a number of other authors have shown that the roughness Reynolds number formed with the roughness height and the flow properties at the edge of the boundary layer,

$$Re_k = \frac{\rho_e u_e k}{\mu_e} \tag{9}$$

is an important parameter which correlates the effect of roughness-induced boundary layer transition over a range of local Mach numbers from 0 - 8.5. Other researchers[20] use the roughness Reynolds number based on the roughness height and the flow properties at the top of the roughness element. **Figure 13** shows the effect of both Mach number and trip position Reynolds number formed with the roughness location and the flow properties at the edge of the boundary layer

$$Re_{x_k} = \frac{\rho_e u_e x_k}{\mu_e} \tag{10}$$

on the effective trip Reynolds number based on the effective roughness height, i.e the roughness height necessary to move transition to the roughness position, and the flow properties at the edge of the boundary layer

$$Re_{k_{eff}} = \frac{\rho_e u_e k_{eff}}{\mu_e}. \tag{11}$$

With a roughness position Reynolds number of $Re_{xk} = 1.9\times10^5$, calculated using the flow properties at the edge of the undisturbed boundary layer at tripping location and the tripping location $x_k = 0.75$ inches, the effective Reynolds number results in $Re_{keff} \approx 1\times10^4$ determined using the correlation in Fig. 13. Thus, the roughness element height was calculated to $k_1 = 0.04$ inches.

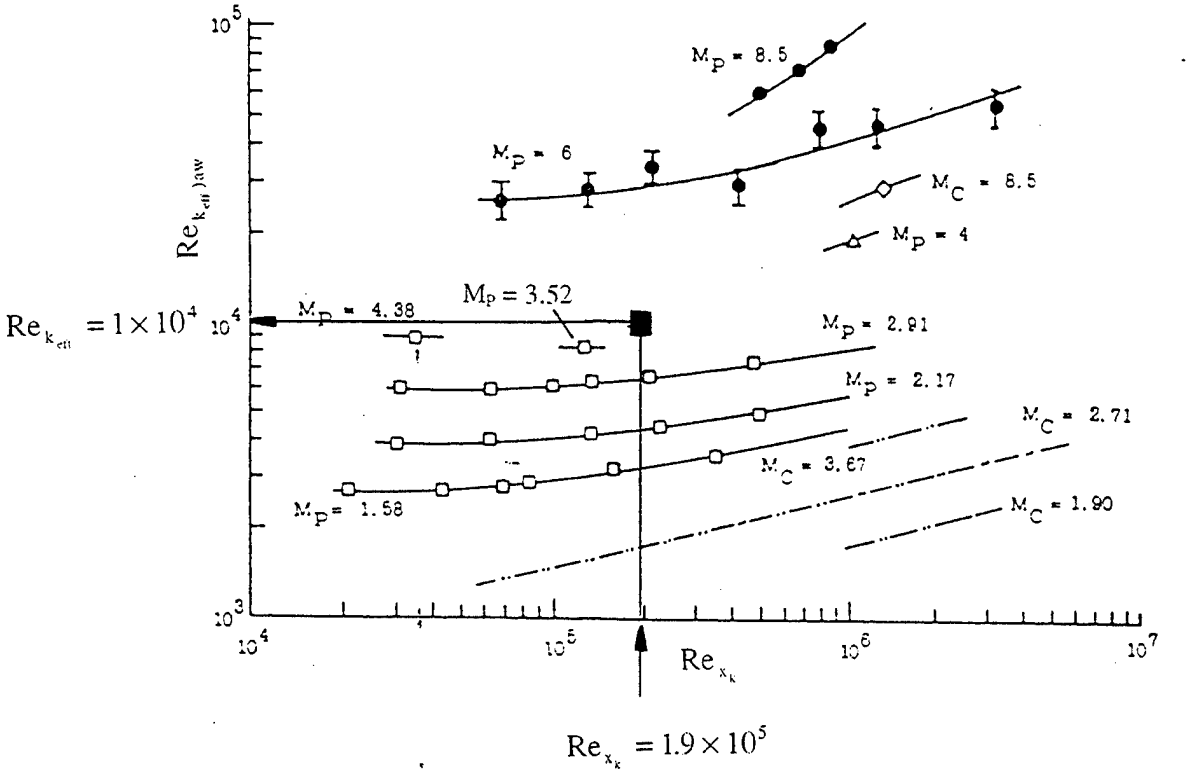

Figure 13: Variation of effective roughness Reynolds number with roughness position Reynolds number and Mach number for spherical roughness elements at adiabatic wall conditions as taken from Morrisette[21] (M_P: local Mach number for a flat plate, M_C: local Mach number for a cone)

Size of tripping devices

As reported in Sterret[18] roughness elements cause undesirable spanwise distortion of the flow. If the roughness elements are of proper size (in his investigations $k/\delta_k \approx 2$) spanwise distortions of the flow is very slight which results in a uniform spanwise flow close to the roughness elements indicating the beginning of a turbulent boundary layer. However, if the roughness elements are chosen too high (in his investigations $k/\delta_k > 5$) spanwise distortion can extend from the tripping location over a long range. With the chosen roughness trip location of $x_k = 0.75$ inches and the roughness element height of $k_1 = 0.04$ inches determined from the correlation above in the present investigations, the tripping size is $k/\delta_k \approx 2.4$, which still avoid significantly distortions of the flow in accordance to Sterret[18].

Spacing of roughness

As investigations[21] show, transition location directly behind the elements is insensitive to roughness spacing over a large range and the spanwise uniformity of the transition location would be affected by roughness elements located to far apart. Additionally, Potter[23] mentioned that at supersonic speeds, if the trip spacing is too small, the transition approaches that for the two-

dimensional trip, which is less efficient than three-dimensional trips. In accordance to these investigations a lateral spacing between the elements of 4 times the width of the element (d = 0.0625 inches, s = 0.25 inches) was chosen for the present investigations.

Type of roughness

The effect of different trip shapes (spheres, prisms, rods, pyramids, cylinders) on transition position has been studied of many researchers. Morrisette[21], for example, reported, that for these kinds of trips the effect of trip shape on transition position appeared to be no significant at supersonic speeds. To keep the manufacturing of the elements simple cylindrical roughness elements with spherical heads were chosen. The base of the elements was built with a thread allowing the replacement of the trips against other type of roughness element without modifying the API model. A sketch of the trips used in the present investigation and the locations on the model are shown in **Fig. 14**.

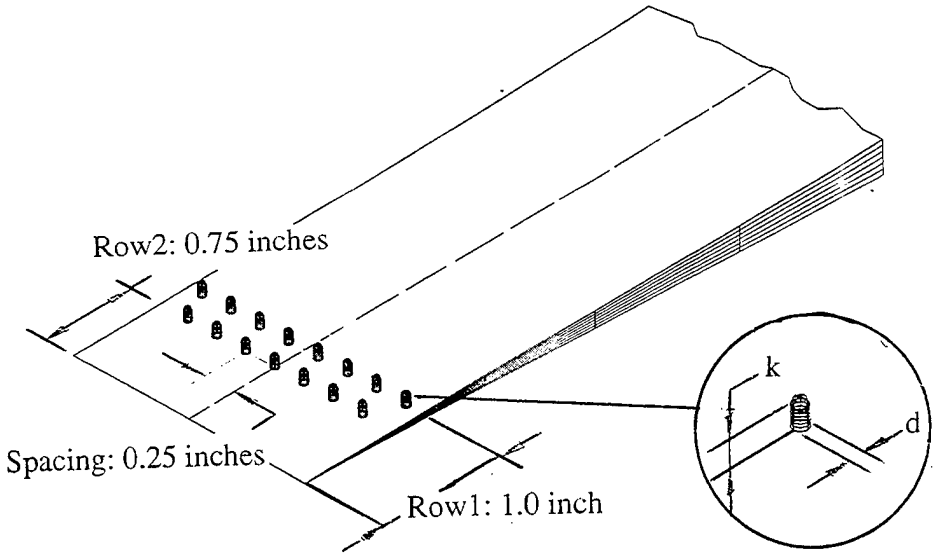

Figure 14: Sketch of the roughness elements and the location on the API model.

Wall temperature and Pressure Gradient

Since the presented investigations covers only boundary layer transition fixing on the lower side of the API model, the effect of wall temperature and pressure gradient is not discussed here.

Figure 15 and Table 4 show the values of the roughness-transition parameters used in the present investigation. Note that the boundary layer thickness δ of the undisturbed flow calculated using GASP at the roughness location was determined by using the total enthalpy as indicated in Fig 15.

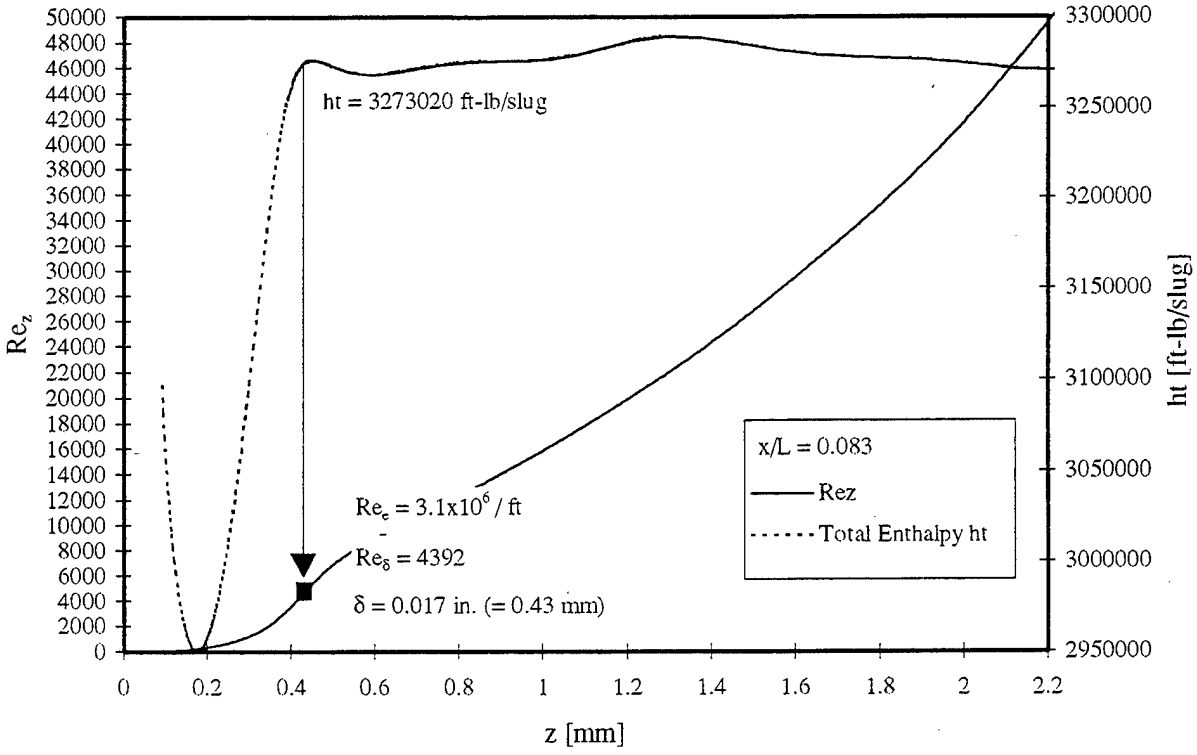

Figure 15: Dimensions of roughness transition parameters

Table 4: Values of roughness-transition parameters

Parameter	Value	Unit
k_1	0.04	in.
d_1	0.0625	in.
x_k	1.00	in.
$Re_e = \frac{\rho_e u_e}{\mu_e}$	3.1×10^6	/ ft
$Re_{k1} = \frac{\rho_e u_e k_1}{\mu_e}$	1×10^4	-
$Re_{xk} = \frac{\rho_e u_e x_k}{\mu_e}$	2.58×10^5	-
$Re_{keff} = \frac{\rho_e u_e k_{eff}}{\mu_e}$	1×10^4 (obtained from correlation in Fig. 13	-
$Re_1 = \frac{\rho_1 u_1}{\mu_1}$	1.68×10^6	/ ft

4.2.2 Results of investigation

Before the effect of roughness-disturbed flow on the transition location on the lower side of the API model is discussed, the onset on natural transition will be determined. As reported[21,32] pitot pressure data measured within the boundary layer near the surface can be used to determine the state of the boundary layer. Since the probe diameter used in this study is nominally 2.5 times the computed boundary layer thickness, it has been shown that this instrument is invalid for this flow region. Thus, heat transfer surface measurements were used to determine the begin of the natural transition. **Fig. 16a** shows the surface temperature pattern approached after 21 seconds test duration, ranging with a 5 °C bandwidth from a color play starting at 13 °C and ending at approximately 18 °C.

The beginning of transition is defined as the location where the lowest heat transfer coefficient occurs[12]. Since the TLC indication will approach the lowest level of heat transfer (also highest temperature) the beginning of transition will be disappearing last through the liquid crystal temperature range, leaving the model with a black appearance. On the other hand, if the heat transfer coefficient reaches the highest value (also lowest temperature), the transition process is ended.

Heat transfer coefficients in form of Stanton number along the centerline on the lower side of the API-II model without roughness trips, as shown in **Fig. 16b**, show that the lowest level of heat transfer, i.e. the beginning of the transition region, appears approximately between 28 to 38 percent of the model length. Since the heat transfer coefficient further increase with increasing x/L, transition is assumed to extend beyond the end of the model. However, to what extent the boundary layer tends to re-laminarize due to the presence of the adverse pressure gradient at the compression ramp (staring at x/L = 0.5) has not been investigated in the present study. To clarify the influence of the adverse pressure gradient on the transition process, additional investigations on a flat plate model with- and without compression ramps has to be carried out. Noise and other flow disturbances existing in wind tunnel tests can also influence the transition process. The effect of these parameters on the transition has also not been considered here.

Since the location of natural transition for the test conditions used has been determined, the goal of the further investigation is to move transition forward using trip devices. As mentioned previously, the use of too large roughness elements can significantly influence the inviscid flow field. To investigate the influence of the trip size on the inviscid flow field, static pressures measurements and pitot pressure measurement normal to the surface along the centerline with and without trips were accomplished. As shown in Fig. 8, the static pressures along the centerline starting from the second pressure orifice do not change greatly although shocks are observed at the roughness element. A normal shock, occurring in front of every roughness element, changes to an oblique shock and finally almost evolves into a weak Mach wave. For this reason and that the extent of the shock is too small the measured static pressures do not change. However, the pressure values measured at the first pressure orifice indicate a pressure rise from $p/p_1 = 1.7$ without trips to 3.5 with a trip size of h = 0.08 inches. Since the local Mach number at the location x_k increases with increasing distance from the surface (at least for the conditions used in the present tests), larger roughness elements create stronger normal shocks which cause higher

static pressures right behind the roughness elements. **Figure 17** shows pitot pressure profiles measured normal to the surface at several location of the rear part of the model. Although the largest roughness elements arranged in two rows were used the pitot pressure in the external flow barely changes, indicating that the viscous flow in the aft part of the model is hardly influenced by the trip induced pertubations.

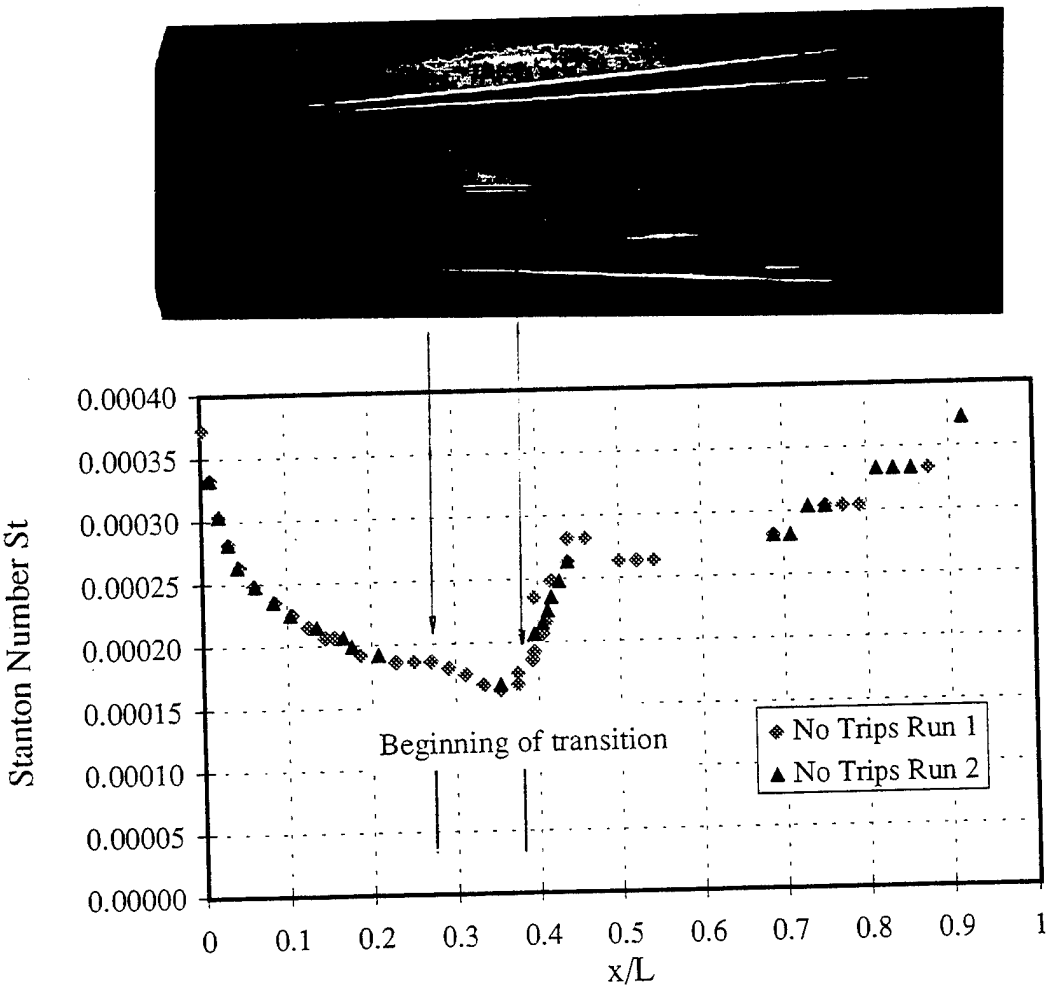

Figure 16: (a) Thermochromic Liquid Crystal (TLC) utilized on the lower forebody surface of the API-II model (b) Heat transfer rates showing the beginning of boundary layer transition (p_{t1} = 200 psia, T_w = 287 K, T_r = 256 K, $T_{w,a}$ = 295 K)

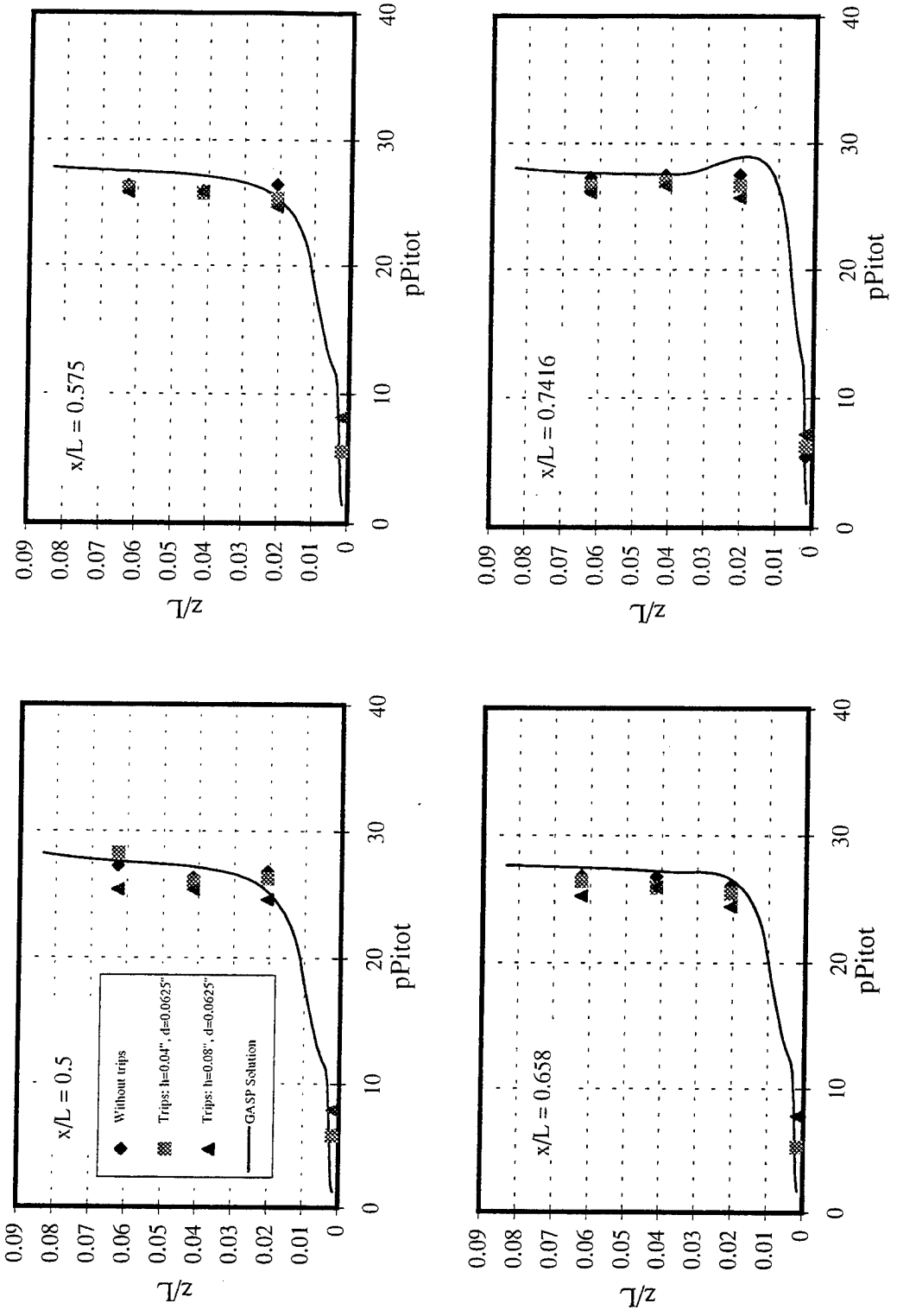

Figure 17: Pitot pressure profiles normal to the surface along the centerline located at the aft part of the model

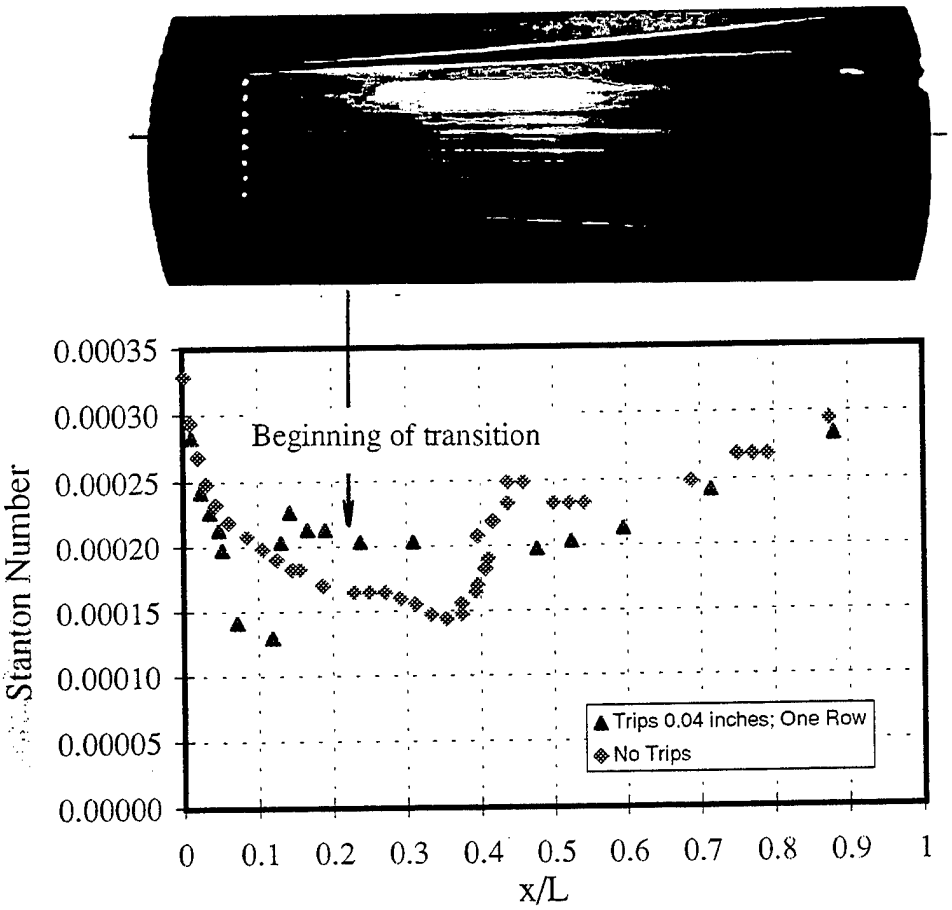

Figure 18: (a) Thermochromic Liquid Crystal (TLC) utilized on the lower forebody surface of the API-II model with roughness elements (b) Stanton number distribution showing the beginning of boundary layer transition (p_{t1} = 200 psia, T_w = 287 K, T_r = 256 K, $T_{w,a}$ = 295 K)

Fig. 18b shows the Stanton number distribution along the centerline on the lower side with roughness trips of h = 0.04 inches in comparison to the Stanton number distribution obtained without trips. It shows that the beginning of trip induced transition moves further upstream and appears at approximately 22 percent of model length. The transition point that might be inferred from normal interpretation of the Stanton-number data on Fig. 18 at x/L≈0.11 is not the true transition point because the flow behind the trips is weakly separate. This separation gives a false indication of transition from the heat transfer measurement. The striation pattern on the surface of the model caused by trip induced vortices indicates a transitional flow as described in Fig 12. Since a break down of the vortices is not visible, the boundary is assumed to be transitional, not turbulent at the rear of the model. This can also be verified by the Stanton number distribution which shows an increase with increasing x/L. In other words, the results show that it was

possible to move the roughness induced transition forward, closer to the tripping elements but a fully turbulent boundary layer in front of the inlet face did not develop.

For this reason, a series of different roughness element sizes arranged in one and two rows close to the leading edge at the same test condition were carried out. **Table 5** shows the different roughness element sizes and the roughness-induced parameters used.

Table 5: Values of roughness-transition parameters

Size of trips	Number of rows	Re_{xk}	Re_k
0.01	1	2.58×10^5	2583
0.02	1	2.58×10^5	5167
0.04	1	2.58×10^5	1×10^4
0.08	2	1.94×10^5 / 2.58×10^5	2×10^4
0.04	2	1.94×10^5 / 2.58×10^5	1×10^4
0.04	2	1.94×10^5 / 2.58×10^5	1×10^4

Figure 19 shows the Stanton number distributions along the centerline of the API-II model for different roughness elements arranged in one and two rows. For all roughness element sizes, even the smallest one, the artificial transition moves further upstream close to the tripping locations. Since the heat rates increase with increasing x/L, the boundary layer is assumed to be transitional beyond the model end. For the test conditions and tripping sizes and locations used, a turbulent boundary layer in front of the inlet face is not to be expected. The use of two rows of tripping devices shows an increase in the heat rates, but a turbulent boundary layer did also not develop. How the adverse pressure gradient at the compression ramp adversely triggers the character of the boundary has not been investigated yet.

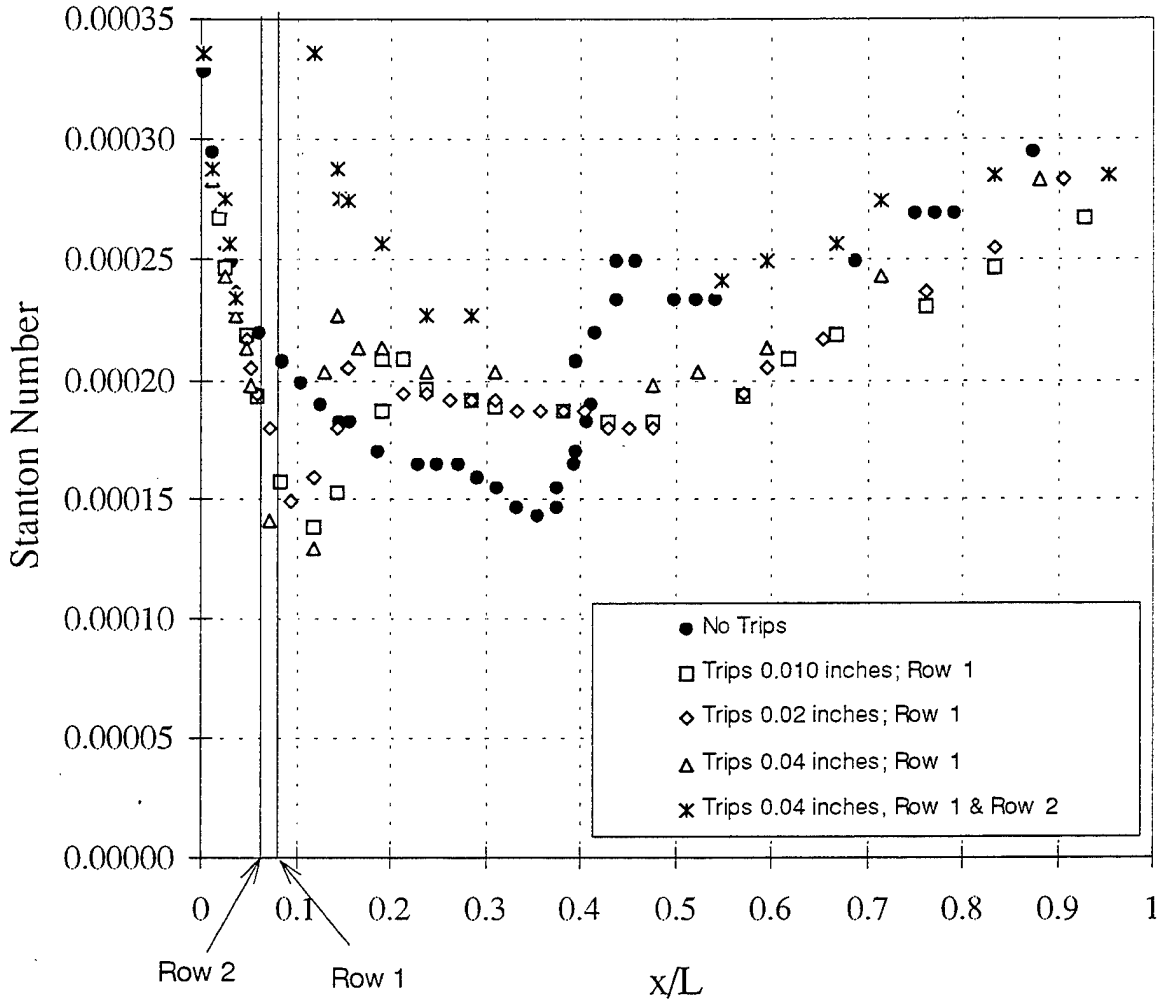

Figure 19: Stanton number distributions along the centerline of the API-II model for different roughness elements arranged in one and two rows (p_{t1} = 200 psia, T_w = 287 K, T_r = 256 K, $T_{w,a}$ = 295 K)

5. Conclusions

A hypersonic Airframe/Propulsion Integration wind tunnel model was designed and tested at the U. S. Air Force Academy to investigate the effect of boundary layer trip-generated vortical flow structures on the development of boundary layer transition, and on interactions with the inviscid external flow. Surface-pressure measurements, pitot pressure measurements, oil flow-visualization photographs and heat transfer distributions were obtained for a Mach 4.28 air stream with a free stream Reynolds number of approximately one million per inch at zero angle of attack. The experimental data were compared with computational results calculated using the General Aerodynamic Simulation program. The following conclusions and recommendations are made:

Conclusions:

- The test results show that for the model geometry used in this study, the inviscid external flow approaching the inlet face is nearly two-dimensional.
- Heat transfer measurements on the bottom surface of the basic model using transient liquid-crystal technique show that natural transition is approximately between 28 to 38 percent of the model length.
- Using the roughness elements, transition began right after the roughness location, and the boundary layer stayed transitional over the remaining model length. A vortical flow induced by the trip elements exists in a region close to the surface at the inlet face.
- For this study, the pitot probe diameter was nominally 2.5 times the computed boundary layer thickness, and thus, was an invalid instrument for determining the state of the boundary layer. In order to measure the total pressures needed to determine the transition location the tube diameter should be a fraction of the boundary layer thickness. Since the boundary layer thickness for the conditions used in this study is very small, this requires placement of the pitot tube to be very near the wall, which may cause interactions between the tube and the wall. Thus, this method is not appropriate for determining the state of the boundary layer.

Recommendations:

- For the verification of the results obtained in this study, other methods for determination of the state of the boundary layer should be used. Such methods could be: (1) Thermocouples located along the centerline (2) Non intrusive optical methods such as holographie interferometry, infrared thermography and Planar Laser Induced Fluorescence.
- The compression ramp in the aft part of the API model causes an adverse pressure gradient which might re-laminarize the transitional boundary layer. To investigate the effect of this pressure gradient on transition, tests on flat plates with and without compression ramps should be carried out. Flat plate flow fields are not strictly two-dimensional in the central section, so heat flux distributions measured along the central axis should be compared with the measured heat rates using flat plates with side plates.
- In addition to the boundary layer trips located near the leading edge of the model, gas injection methods might be used near the nose to also control the onset of boundary layer transition.

6. References

1. Wilson, G. J., Davis, W. H., "*Hypersonic Forebody Performance Sensitivities Based on 3D Equilibrium Navier-Stokes Calculations*". AIAA 88-0370, AIAA 26th Aerospace Sciences Meeting, Jan. 11-14, 1988, Reno, NV.
2. Berens Thomas M.; Bissinger Norbert C.; *Study on Forebody Precompression Effects and Inlet Conditions for Hypersonic Vehicles*. AIAA 96-4531, AIAA 7th International Planes and Hypersonic Systems and Technologies Conference, Norfolk, VA, Nov. 18-22, 1996.
3. Newberry, C. F.; Dresser, H. S. Byerly J. W. Riba W. T.: *The Ecaluation of Forebody Compression at Hypersonic Mach Numbers*. AIAA 88-0479, AIAA 26th Aerospace Sciences Meeting, Jan. 11-14, 1988, Reno, NV.
4. Sommerfield D.; Dao S. C., Schwatrz M.; Wai J. C.. rry, C. F.; *Hypersonic CFD Analysis of Generic Forebodies*. AIAA 88-0372, AIAA 26th Aerospace Sciences Meeting, Jan. 11-14, 1988, Reno, NV.
5. AeroSoft, Inc., Blacksburg, VA 24060, "*General Aerodynamic Simulation Program version 3 User's Manual*", May 1996.
6. Pope, A.; Goin K. L.: *"High-Speed Wind Tunnel Testing"*, John Wiley & Sons, Inc., New York, 1965.
7. Buch, G.; Lee, T; Scott M.: *"A Pressure Measurement Uncertainty Investigation in the Tri-Sonic Wind Tunnel"*, 471-Project, DFAN, Spring 1997.
8. Coleman, H. W., Steele, W. G., *Experimentation and Uncertainty Analysis for Engineers*, John Wiley & Sons, Inc., Ney York, NY, 1989.
9. Standard, *Assessment of Wind Tunnel Data Uncertainty*, Washington, DC 20024, AIAA S-071-1995.
10. Beckwith, Th. G., Marangoni, R. D., Lienhard V, J. H. *Mechanical Measurement*. 5th ed., Addison-Wesley Publishing Company, New York 1993.
11. Kline, S. J., and McClintock, F. A., "Describing Uncertainties in Single-Sample Experiments", Mechanical Engineering, Vol. 75, Jan. 1953, pp. 3-8.
12. Bertin, J. J., Hypersonic Aerothermodynamics, AIAA Education Series, Washington, D. C., 1994.
13. Ames Research Staff, "Equations, Tables, and Charts for Compressible Flow", NACA Report 1135, 1953.
14. Ireland, P. T., Wang, Z., and Jones, T. V., "Liquid Crystal Heat Transfer Measurements", MEASUREMENT TECHNIQUES, Lecture Series 1995-01, von Karman Institue for Fluid Dynamics, Oxford University, United Kingdom.

15. Babinski, H., Edwards J. A., "Automatic liquid crystal thermography for transient heat transfer measurements in hypersonic flow", Experiments in Fluids, No. 21, pp. 227-236.

16. Pointwise, Inc., Bedford, Texas 76095, "*Gridgen versin 12 User's Manual*", July 1997.

17. McCauley, W. D., Saydah, A., and Bueche, J., "*The effect of controlled three-dimensional roughness on hypersonic laminar boundary layer transition*" AIAA Paper No. 66-26, Jan. 1966

18. Sterrett James R.; Morrisette Leaon E.; Whitehead Allen H., Jr.; Hicks Raymond M.: *Transition Fixing for Hypersonic Flow.* NASA TN D-4129.

19. Braslow Albert L.: *Review of the Effect of Distributed Surface Roughness on Boundary Layer Transition.* AGARD Report 254 April 1960.

20. Braslow Albert L.: *A Review of Factors Affecting Boundary Layer Transition.* NASA TN D-3384, August 1966.

21. Morrisette, Leon E.; Stone David R.; Whitehead Allen H. Jr.: *Boundary-Layer Tripping with Emphasis on Hypersonic Flows.* C. S. Wells (ed.), Viscous Drag Reduction, Plenum Press, Ney York, 1969

22. Potter J. Leith, Whitfield Jack D.: *Effects of slight nose bluntness and roughness on boundary-layer transition in supersonic flow.* Journal of Fluid Mechanics, V. 12,1962, Cambridge at the university press. Pt. IV, pp. 501-535.

23. Potter J. Leith, Whitfield Jack D.: *Boundary-Layer Transition under Hypersonic Conditions.* AGARDograph 97, Pt. III, pp. 1-61, May 1965.

24. Schlichting, H.: "Boundary layer Theory", McGraw Hill, Series in Mechanical Engineering, 7th edition, 1979.

25. Klebanoff, P. S., Schubauer, G. B., and Tidstrom, K. D., "Measurement of the effect of two - dimensional and threedimensional roughness elements on boundary-layer transition," Readers' Forum, National Bureau of Standards, Washington, D. C., June 1955.

26. Westkaemper, J. C., "turbulent boundary-layer separation ahead of cylinders," AIAA Journal, Vol 6, No. 7, 1352-1355, July 1968

27. Smith A. M. O., Clutter, D. W.: "The smallest Height of Roughness Capable of Affecting Boundary-Layer Transition," Journal of the Aero/Space Sciences, pp.229-245, April 1959.

28. Wuest, W.: "Strömungssonden, Teil I. Gesamtdrucksonden (Pitotrohre) (Flow probes, Part I. Total pressure probes (Pitot tubes)). Archiv für Technisches Messen, V 116-9, Lieferung 299 (1960), pp. 245-248

29. MacMillan, F. A.: "Viscous Effects on Flattened Pitot Tubes at Low Speeds," J. Roy. Aeron. Soc. 58 (1954), pp. 837-839.

30. Arnal, D., "Laminar-Turbulent Transition", TKS Murphy, Computational Methods in Hypersonic Aerodynamics, Kluwer Academic Publishers, 1991.

31. Schultz, D.L. and Jones, T.V, "Heat Transfer Measurements in Short Duration Hypersonic Facilities," AGARD-AG-165, February 1973.

32. Schlichting, H., "Boundary-Layer Theory", McGraw-Hill Series in Mechanical Engineering, 1979